

**Two-pulse interference and correlation in an attoclock**Anatoli S. Kheifets <sup>1,\*</sup>, Joshua Cesca <sup>1</sup>, Vladislav V. Serov <sup>2</sup>, Kyung Taec Kim,<sup>3,4</sup> and Igor A. Ivanov<sup>3</sup><sup>1</sup>*Research School of Physics, The Australian National University, Canberra Australian Capital Territory 2601, Australia*<sup>2</sup>*Department of Theoretical Physics, Saratov State University, 83 Astrakhanskaya, Saratov 410012, Russia*<sup>3</sup>*Center for Relativistic Laser Science, Institute for Basic Science, Gwangju 61005, Korea*<sup>4</sup>*Department of Physics and Photon Science, GIST, Gwangju 61005, Korea*

(Received 3 June 2021; revised 1 September 2021; accepted 14 September 2021; published 29 September 2021)

We study cross correlation of a single-cycle circularly polarized laser pulse with its delayed and/or attenuated replica in the attoclock field configuration. In this configuration, tunneling ionization of the target atom is observed in the polarization plane of the driving laser pulse. The two-pulse attoclock displays a robust interference pattern in the photoelectron energy spectrum and the real time correlation between the photon absorption rates from the two pulses. This interference and correlation can be used for characterization of single-cycle laser pulses and monitoring the target population dynamics during the ionization process.

DOI: [10.1103/PhysRevA.104.033118](https://doi.org/10.1103/PhysRevA.104.033118)**I. INTRODUCTION**

Electron interference goes to the core of wave-particle duality. Electrons driven by strong laser pulses follow different trajectories and their multiple quantum paths interfere [1]. Quintessential strong field ionization phenomena, such as high-order harmonics generation [2–4] and above threshold ionization (ATI) [5–7] give ample examples of such interference. ATI by itself arises from interference between electrons emitted during different cycles of a long laser pulse [8]. When the driving pulse becomes short, the ATI interference fringes are washed out. This is typical in attoclock experiments aiming to resolve tunneling time [9–13].

The attoclock employs a slightly elliptical multicycle laser pulse to tunnel ionize an atom. When the laser field is at its maximum (here we assume it directed vertically along the  $\hat{y}$  axis), the initially bound atomic electron enters the tunnel at  $t = t_{\text{in}}$  to traverse the potential barrier. This electron exits the tunnel at  $t = t_{\text{out}}$  with zero velocity. At this instant, it records the vector potential of the laser field and carries it to the detector. If the tunneling is instantaneous, the vector potential at the exit point is directed horizontally (along the  $\hat{x}$  axis). If the tunneling takes real time  $\tau_T = t_{\text{out}} - t_{\text{in}}$ , the vector potential and the photoelectron momentum at the detector  $k_{t \rightarrow \infty}$  rotate by the angle  $\theta_A = \omega\tau_T$ . Thus, the attoclock performs a time-to-angle conversion with the proportionality coefficient being the carrier frequency. An alternative interpretation [8,14] suggests a purely imaginary tunneling time  $t_{\text{in}} = t_{\text{out}} + i\tau_T$ ,  $\tau_T = \gamma/\omega$ ,  $\gamma \ll 1$  is the Keldysh parameter in the tunneling regime. Meanwhile the attoclock rotation angle is entirely due to the Coulomb field of the ion remainder [15]. A finite tunneling time is a subject of considerable debate at present [16–18].

The attoclock setup can be used to study photoelectron interference caused by a sequence of two circularly polarized laser pulses. Bicircular fields of the same or different colors cause intricate vortex structures in the photoelectron momentum distribution projected on the polarization plane. These structures have been predicted theoretically [19–21] and later observed experimentally [22,23].

In the present paper we employ a sequence of two single-cycle circular pulses to revive the ATI fringes in the photoelectron spectrum and to build an attoclock interferometer. Such an interferometer is very robust and can be used to characterize single-cycle laser pulses by cross correlation of the master and delayed replica pulses. An additional correlation of these two pulses can be studied directly by detecting the rates at which the photons are absorbed at different times. These two methods provide the means for accurate characterization of single-cycle laser pulses. Multiple useful applications of such pulses are well documented [24,25]. In addition, the two-pulse attoclock interference can be used for monitoring the target population dynamics during the ionization process.

The rest of the paper is organized into the following sections. In Sec. II we outline the basic theory of two-pulse interference. In this section we follow closely the discussion and the formalism developed by Della Picca *et al.* in Ref. [26]. In Sec. III we describe our simulations based on the numerical solution of the time-dependent Schrödinger equation (TDSE) (III A), utilizing the saddle-point method (III B) and employing the time-correlation analysis (III C). Our numerical results are presented in Sec. IV. Finally, we conclude in Sec. V by outlining further possible extensions of the present study.

**II. TWO-PULSE INTERFERENCE**

The two photoelectron wave packets emitted by a sequence of two laser pulses interfere at the detector with the resulting

\*A.Kheifets@anu.edu.au

probability,

$$P = |T_1|^2 + |T_2|^2 + 2|T_1||T_2| \cos \Phi. \quad (1)$$

Here  $T_1$  and  $T_2$  are the magnitudes of the two photoelectron wave packets, and  $\Phi$  is their relative phase shift expressed as [26]

$$\begin{aligned} \Phi = & \frac{N_1\pi}{\omega} \left( I_p + \frac{k^2}{2} + U_{p1} \right) + \frac{N_2\pi}{\omega} \left( I_p + \frac{k^2}{2} + U_{p2} \right) \\ & + \Delta t \left( I_p + \frac{k^2}{2} \right) + \frac{k}{\omega^2} (F_1 - F_2). \end{aligned} \quad (2)$$

Here  $k$  is the photoelectron momentum,  $I_p$  is the ionization potential of the target atom,  $\omega$  is the base laser frequency, and  $N_1, N_2$  are the number of cycles in the first and second flattop pulses. The time separation between the two pulses is denoted by  $\Delta t$ . The quantity,

$$U_p = \frac{1}{T} \int_{t_i}^{t_i+T} \frac{|A(t')|^2}{2} dt' = \frac{F^2}{(2\omega)^2} \quad (3)$$

is known as the ponderomotive energy which can be expressed via the peak electric-field strength  $F$ . Here and throughout, we adopt the atomic units and set  $e = m = \hbar = 1$ . For a long flattop laser pulse,  $U_p$  becomes the cycle-averaged kinetic energy of the laser-driven electron. For a pulse with a rapidly varying envelope,  $U_p$  is dependent on time. This effect requires a special consideration as was shown experimentally [6] and theoretically [27].

In the present paper, we consider the special case of two single-cycle pulses  $N_1 = N_2 = 1$ . In this case, Eq. (2) is reduced to

$$\begin{aligned} \Phi = & \left( E + I_p + \frac{U_{p1} + U_{p2}}{2} \right) T + (E + I_p) \Delta t \\ & + \frac{k}{\omega^2} (F_1 - F_2), \quad E = k^2/2, \quad T = 2\pi/\omega. \end{aligned} \quad (4)$$

For the two equal strength laser pulses, the last term in Eq. (4) drops out. The phase (4) and the two-pulse ionization probability (1) are then simplified to

$$\Phi = (E + I_p)(T + \Delta t) + U_p T, \quad (5)$$

$$P \propto 1 + \cos \Phi \propto \cos^2 \Phi/2. \quad (6)$$

The physical meaning of Eq. (5) is particularly simple. In a semiclassical picture, the photoelectron phase can be expressed via the action,

$$\phi = S(t_{in}) = \int_{t_{in}} \left[ \frac{|\mathbf{k} + \mathbf{A}(t')|^2}{2} + I_p \right] dt', \quad (7)$$

where  $t_i$  marks the birth time of the photoelectron. The phase difference  $\Phi = \phi(t_{in1}) - \phi(t_{in2})$  is acquired during the free propagation of the first electron between the pulses and its laser driven propagation during the first pulse. The time integral of the linear term  $\int [\mathbf{k} \cdot \mathbf{A}(t')] dt' = 0$  for a single-cycle pulse (see Chap. 2 of Joachain *et al.* [28]).

When the time interval between the pulses tends to zero, Eq. (5) reduces further to

$$\Phi = (E + I_p + U_p)T. \quad (8)$$

The peaks of the two-pulse ionization probability (6) correspond to phase (8) reaching  $2n\pi$ . Positions of these peaks in the photoelectron spectrum mark the integer numbers of the absorbed photons,

$$E_n = n\omega - I_p - U_p. \quad (9)$$

Noteworthy, Eq. (9) defines the conventional ATI spectrum. Thus, the interpulse interference of two identical single-cycle pulses is similar to the intercycle interference of a flattop multicycle pulse.

### III. METHODS

#### A. Time-dependent Schrödinger equation

We solve numerically a one-electron TDSE,

$$i \partial \Psi(\mathbf{r}, t) / \partial t = [\hat{H}_{\text{atom}} + \hat{H}_{\text{int}}(t)] \Psi(\mathbf{r}, t), \quad (10)$$

where  $\hat{H}_{\text{atom}}$  describes a field-free atom and contains the Coulomb potential (hydrogen), a screened Coulomb potential  $-1.908e^{-r}/r$  (Yukawa) and a localized one-electron potential (argon). Equation (10) is exact for the hydrogen and Yukawa atoms and relies on the single active electron approximation for argon. The interaction Hamiltonian is written in the velocity gauge,

$$\hat{H}_{\text{int}}(t) = \mathbf{A}(t) \cdot \hat{\mathbf{p}}, \quad \mathbf{E}(t) = -\partial \mathbf{A} / \partial t. \quad (11)$$

The vector potential in Eq. (11) is defined via the classical coordinate of the elliptical motion  $\mathbf{A}(t) = \mathbf{r}'(t)$ , where

$$\mathbf{r}(t) = \frac{E_0}{\omega^2 \sqrt{\epsilon^2 + 1}} \sin^4 \left( \frac{\omega t}{2N} \right) \begin{bmatrix} \epsilon \cos(\omega t) \mathbf{e}_x \\ \sin(\omega t) \mathbf{e}_y \end{bmatrix}. \quad (12)$$

The TDSE (10) was solved by two different numerical techniques [29,30] cross-checked against each other. The photoelectron momentum distribution (PMD) was obtained by projecting the solution of Eq. (10) on the basis of scattering states,

$$P(\mathbf{k}) = |\langle \varphi_{\mathbf{k}}(r) | \Psi(\mathbf{r}, t \rightarrow \infty) \rangle|^2. \quad (13)$$

In attoclock measurements, the experimentally observed quantity is the PMD (13) projected on the polarization ( $x, y$ ) plane,

$$P(k_x, k_y) = \int_{-\infty}^{\infty} dk_z P(\mathbf{k}). \quad (14)$$

We also analyze the photoelectron energy spectrum collected from all the emission directions,

$$P(E) = \int k d\Omega_k P(\mathbf{k}), \quad E = k^2/2. \quad (15)$$

#### B. Strong-field approximation and saddle-point method

We adopt the saddle-point method (SPM) [8] which relates the photoelectron momentum at the detector  $\mathbf{k}_{t \rightarrow \infty}$  with a specific instant of tunneling  $t_{in}$  such that the semiclassical action along the photoelectron trajectory starting from this instant,

$$S_{\mathbf{k}}(t) = \int_{t_{in}}^t dt' \{ [\mathbf{k} + \mathbf{A}(t')]^2 / 2 + I_p \} \quad (16)$$

is stationary,

$$\partial S_k(t_{\text{in}})/\partial t = [\mathbf{k} + \mathbf{A}(t_{\text{in}})]^2/2 + I_p = 0. \quad (17)$$

In a general case, several solutions of Eq. (17) lead to the final photoelectron momentum  $\mathbf{k}$ , and the PMD is given by the sum over the corresponding tunneling ionization times [31]. With exponential accuracy,

$$P(\mathbf{k}) \propto \sum_{t_{\text{in}}}^{N_{\text{SP}}} |S_k''(t_{\text{in}})|^{-1} \exp[iS_k(t_{\text{in}})]^2. \quad (18)$$

For few-cycle circularly or elliptically polarized laser pulses, the number of saddle points for a given momentum is  $N_{\text{SP}} = N + 1$  [32]. The solving of Eq. (17) and the evaluation of Eq. (18) was carried out using the nonlinear optimization program suite [33].

### C. Time-correlation analysis

We define the time-correlation function for the Heisenberg operator of the number of absorbed photons  $\hat{N}(t)$  acting on the initial atomic state  $\phi_0$  as [34]

$$C(t_2, t_1) = \langle \phi_0 | \hat{N}(t_2) \hat{N}(t_1) | \phi_0 \rangle. \quad (19)$$

A similar Heisenberg representation was employed in our earlier works to study auto-correlation functions of the coordinate and momentum operators [35] and the operator of the instantaneous ionization rate [36]. Actual computations of the autocorrelation function (19) are conducted in the Schrödinger representation,

$$C(t_2, t_1) = \langle \hat{U}(t_2, 0) \phi_0 | \hat{N} \hat{U}(t_2, t_1) \hat{N} \hat{U}(t_1, 0) \phi_0 \rangle, \quad (20)$$

where  $U(t_2, t_1)$  is the propagator driving the atom and the field from  $t_1$  to  $t_2$ . These computations are reduced to multiple solutions of the TDSE (10) as explained in Ref. [35]. The correlation between the rates at which the photons are absorbed at different times is obtained from  $C(t_2, t_1)$  by taking derivatives with respect to  $t_1$  and  $t_2$ .

For the presently employed circularly polarized pulses, the photon number operator  $\hat{N}$  can be replaced with the operator  $\hat{l}_z$  of the angular momentum projection on the propagation axis. Since each photon absorption event results in an increment of  $l_z$  by one unit, the operator  $\hat{l}_z$  can be used to count the number of absorbed photons if we neglect the photon emission process. Thus, the replacement of  $\hat{N}$  with  $\hat{l}_z$  amounts to the well-known rotating-wave approximation. In the present settings, this approximation is fully equivalent to the *ab initio* quantum electrodynamics approach [37].

## IV. RESULTS

### A. Single pulse attoclock

The attoclock principles are illustrated in the top row of panels in Fig. 1. Panel 1(a) displays a multicycle elliptical pulse which is used to tunnel ionize the two atomic targets: the hydrogen and the Yukawa atoms. In the latter model atom, the long-range Coulomb potential is screened whereas keeping the same binding energy as in hydrogen. Fig. 1 displays the photoelectron momentum distribution (PMD) of the Yukawa atom (1b) and hydrogen (1c) atoms projected onto the polarization

plane. The PMD of the Yukawa atom is perfectly aligned in the horizontal direction whereas that of the hydrogen atom is offset by a significant angle. This confirms the Coulombic origin of the attoclock offset angle. Both PMDs display very distinct ATI fringes. In the multicycle pulse shown in Fig. 1(a), the tunneling ionization takes place at several instances (peaks of the electric field), and the photoelectrons are emitted in both directions. The electrons emitted from neighboring electric-field peaks interfere with the phase difference given by Eq. (8). The maxima of the interference fringes occur when  $\Phi = 2n\pi$  which corresponds to an integer number of photons absorbed from the laser field as specified by Eq. (9).

The photoelectron spectrum obtained by the angular integration of the PMD of hydrogen exhibited in Fig. 1(c) is shown in Fig. 2(a). The interference structure matches the expected pattern defined by Eqs. (6) and (8),

$$\cos^2[(E + U_p + I_p)T/2]. \quad (21)$$

However, the predicted interference minima are not fully filled which reflects a finite spectral width of the pulse. In Fig. 2(a) we also display a photoelectron spectrum produced by a shorter pulse with a smaller number of cycles  $N_c = 3$ , compared to the original  $N_c = 10$ . The ATI interference structure is completely washed out with this shorter pulse due to its larger spectral width.

### B. Two-pulse attoclock

#### 1. Identical pulses

On the bottom row of panels in Fig. 1 we display the results of our simulations with a sequence of two identical single-cycle pulses at a variable delay  $\Delta t$  shown in panel Fig. 1(d). The  $N_c = 1$  pulses are so short that photoelectrons are emitted only once during the pulse length. Accordingly, the PMD contains only one lobe of intensity in comparison with two symmetric lobes for a longer pulse. This single lobe is perfectly aligned with the vector potential in the  $\hat{x}$  direction for Fig. 1(e) the Yukawa atom whereas it is offset by a considerable angle for Fig. 1(f) the hydrogen atom. Both PMDs in panels (e) and (f) contain a very distinct interference pattern which is displayed in more detail for the hydrogen atom in Fig. 2. Here the pulse separation is  $\Delta t = 0$  in Fig. 2(b) and  $T/2$  in Fig. 2(c). The interference pattern is matched very accurately by Eqs. (6) and (5),

$$\cos^2[(E + I_p)(T + \Delta t)/2 + U_p T/2]. \quad (22)$$

Although the interference pattern becomes washed out for a single short pulse even for a modest number of cycles  $N_c = 3$ , it is perfectly clear for the two single-cycle pulses. Comparison of Figs. 2(b) and 2(c) shows that the number of interference fringes increases with  $\Delta t$  as expected from Eq. (22) whereas the clarity of the pattern remains the same.

#### 2. Orbital structure effect

The two-pulse interference is insensitive to the orbital structure of the target atom. Here we demonstrate this insensitivity by considering various  $m$  projections of the initial  $3p_m$  state of the Ar atom. It is known that  $3p_m$  photoelectron spectra with various  $m$  projections differ significantly. The

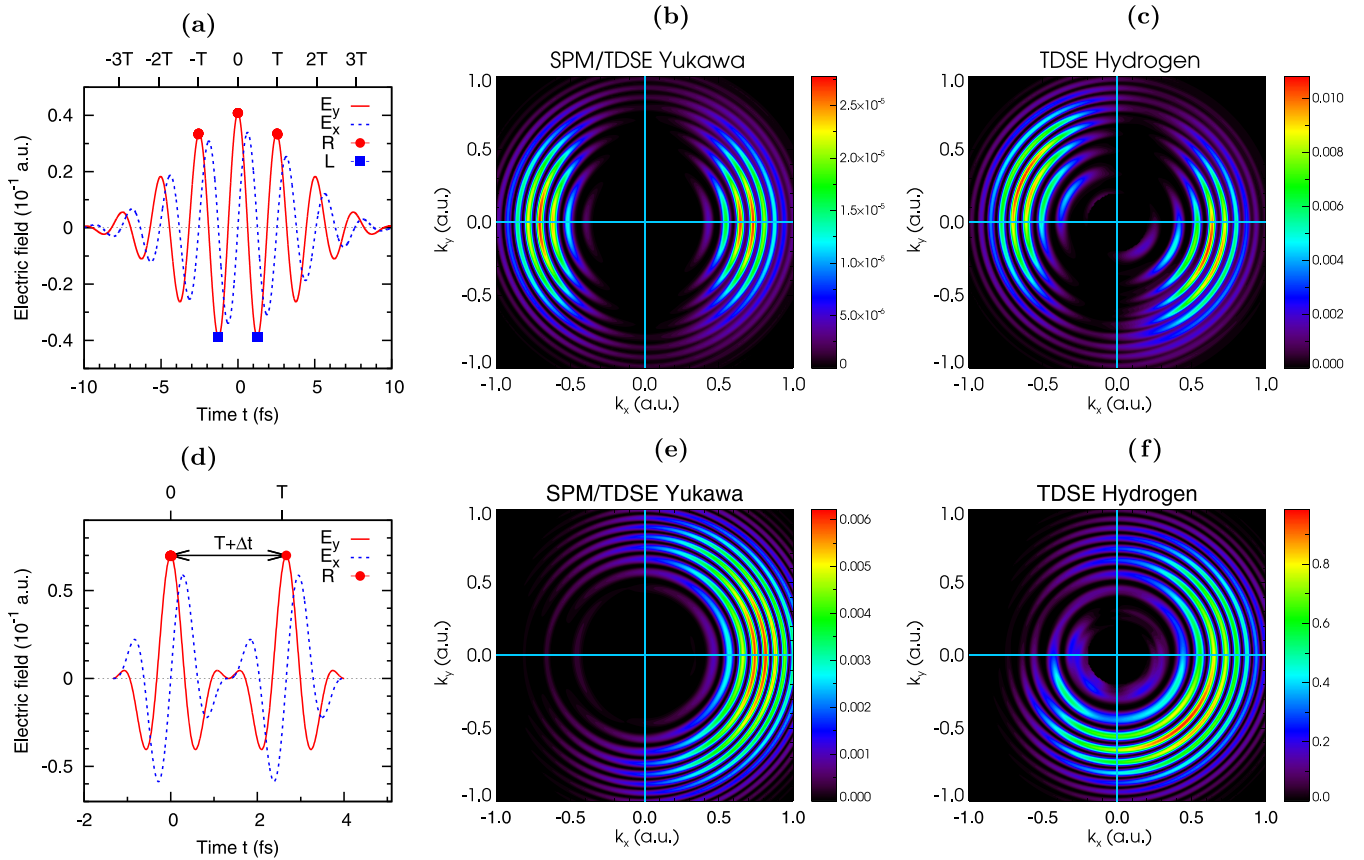


FIG. 1. The electric field of the driving pulse (a) and (d) and the photoelectron momentum distribution in the polarization plane for the model Yukawa atom (b) and (e) and the hydrogen atom (c) and (f). The top panels (a) and (c) correspond to a long  $N_c = 10$  pulse with  $I = 1 \times 10^{14}$  W/cm<sup>2</sup>,  $\epsilon = 0.84$ , and  $\lambda = 790$  nm. In the bottom panels (d)–(f), a sequence of two identical single-cycle pulses is used with  $I = 0.86 \times 10^{14}$  W/cm<sup>2</sup>,  $\epsilon = 1$ , and  $\lambda = 800$  nm separated by  $\Delta t = 0$ . The red circles and blue squares, respectively, on (a) highlight the peak values of the electric field where emission of the photoelectron wave packets takes place receding to the right ( $k_x > 0$ ) and left ( $k_x < 0$ ) in the PMD plot (b). Only the right emission direction is highlighted in (d). The TDSE calculations are used in the PMD plots (b), (c), (e), and (f) whereas for the Yukawa atom (b) and (e) they are indistinguishable (up to a scaling factor) from the SPM calculations.

ionization rate for circularly polarized light counter-rotating with the electron cloud is greatest [31]. Additionally, the orbital momentum projection of the bound electron supplements the total number of photons absorbed from the laser field

causing the photoelectron spectra with different  $m$ 's to peak at different energies [38]. Both these effects can be seen in Fig. 3 where we exhibit the photoelectron spectra of Ar  $3p_m$  produced by a single-cycle pulse and a sequence of two pulses

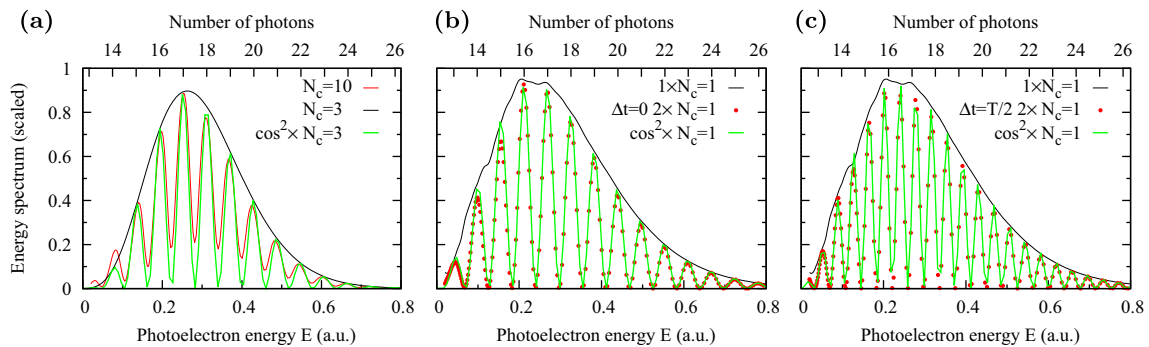


FIG. 2. Photoelectron energy spectra of hydrogen with (a) a long  $N_c = 10$  pulse and (b) two single-oscillation  $N_c = 1$  pulses with an extra separation  $\Delta t = 0$ , and (c)  $\Delta t = T/2$ . The pulse parameters are the same as in Fig. 1. For the long pulse (a), the interference pattern is fitted with a smooth Gaussian function representing the  $N_c = 3$  spectrum and is modulated by Eq. (21). The number of absorbed photons  $(E + I_p + U_p)/\omega$  is marked on the top axis. For the sequence of two single-cycle pulses, the interference pattern is fitted with a smooth Gaussian envelope of a single  $N_c = 1$  pulse modulated by Eq. (22).

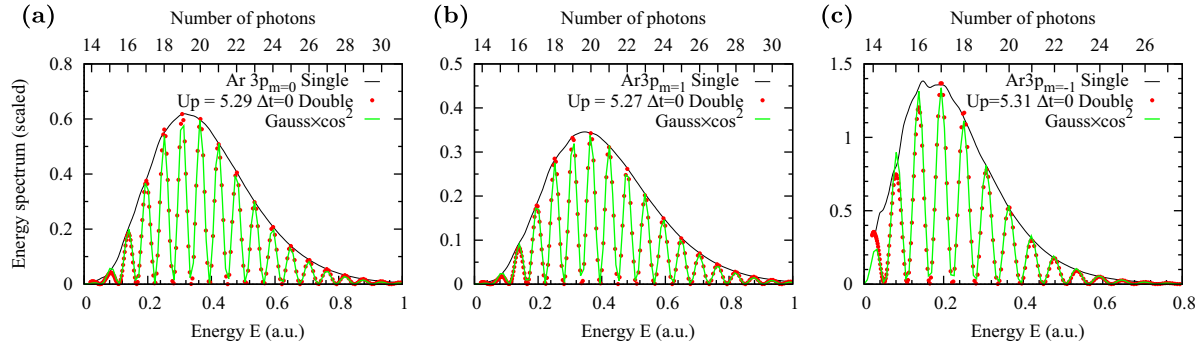


FIG. 3. Photoelectron energy spectra of the argon  $3p$  shell driven by two single-oscillation pulses with  $I = 0.86 \times 10^{14}$  W/cm $^2$ ,  $\epsilon = 1$ , and  $\lambda = 800$  nm separated by  $\Delta t = 0$ . The interference pattern is fitted with a smooth Gaussian envelope of a single pulse modulated by Eq. (22). The panels (a)–(c) correspond to the  $3p_m$  initial states with  $m = 0, 1$ , and  $-1$ , respectively. The corresponding  $U_p$ 's are marked in each panel.

separated from peak to peak by a period with  $\Delta t = 0$ . Despite the clear distinctions between the individual  $m$  spectra, the interference pattern is invariably the same as described by Eq. (22). This was verified by using  $U_p$  as a fitting parameter and the resulting values for various  $m$ 's (marked in Fig. 3) differ only in the third significant figure.

### 3. Reduced second pulse

So far we analyzed the two-pulse attoclock results with two identical pulses whereas delaying the trailing pulse. Equations (1) and (4) allow us to consider a more general case of the two pulses of different intensity. This case is illustrated in Fig. 4 where the intensity of the leading pulse at  $0.86 \times 10^{14}$  W/cm $^2$  is scaled down by a factor of  $\nu \leq 1$  in the trailing pulse. The effect of the second pulse reduction is very bold. Not only do the interference maxima shift away from the integer number of absorbed photons, more vividly, the interference minima become only partially filled. This effect is obvious from Eq. (1) in which  $|T_1|^2 + |T_2|^2 \geq 2|T_1||T_2|$  whereas the equal sign corresponds to the special case of the two pulses of the same intensity. When applying Eq. (1), we assume an exponential reduction in the tunneling ionization rate.

### 4. Inverted second pulse

So far we demonstrated the sensitivity of the two-pulse interference to the individual pulse intensities which affect their corresponding ionization amplitudes and the ponderomotive energies. The effect of the electric-field wave-

form on the two-pulse interference is more subtle. In this section we demonstrate this effect by inverting the polarity of the trailing pulse as is displayed in Fig. 5(a). By doing so we allow the photoelectrons to be ejected both to the left and to the right in a similar way to the long multicycle pulse exhibited in Fig. 1(b). Accordingly, the PMDs displayed in Fig. 5(b) at  $\Delta t = 0$  acquires two symmetric lobes. Not only that, a sizable probability exists for the photoelectron to be emitted along the  $\hat{y}$  axis. Although the interference pattern is very weak along the  $\hat{x}$  axis, it is strongly pronounced along the  $\hat{y}$  axis. This can be seen more clearly from the momentum density cut  $P(k_x = 0, k_y)$  exhibited in Fig. 5(c). Such behavior can be explained by the electric-field diagram of Fig. 5(a). Indeed, the photoelectrons emitted to the left and right hardly interfere. At the same time, the electrons emitted in the vertical directions are produced during the two peaks of the field which are separated by noticeably different  $\Delta t_{E_x > 0} < \Delta t_{E_x < 0}$ . Accordingly, the spacing of the interference fringes is changed as prescribed by Eq. (22). It is always greater for  $k_y < 0$  than for  $k_y > 0$  as is illustrated in Fig. 5(c) for  $\Delta t = 0$ . A similar effect can be seen in the hydrogen atom (not shown here) whose PMD is offset from the  $\hat{x}$  axis as in panels (c) and (f) of Fig. 1.

### 5. Two-pulse time correlation

Another cross-correlation technique that can be used in the attoclock settings is a real time correlation between the photon absorption rates from the two single-cycle pulses. This

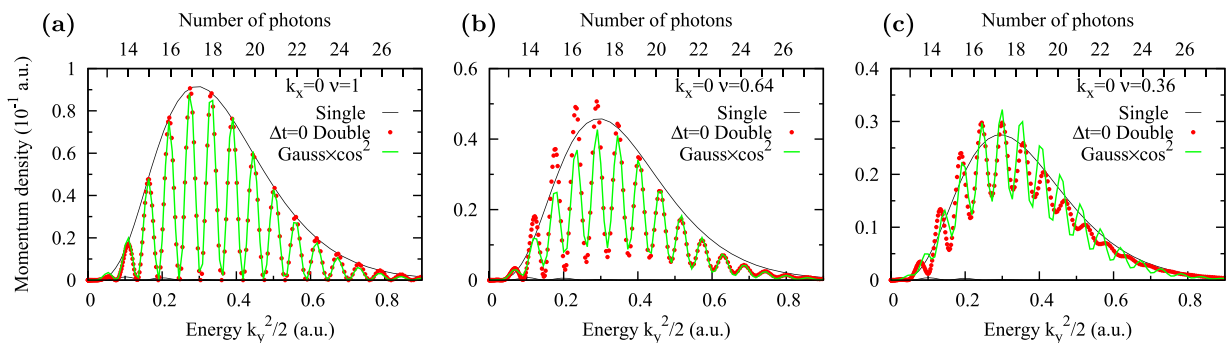


FIG. 4. Two-pulse interference in the Yukawa atom with the two scaled pulses. Intensity of the leading pulse at  $0.86 \times 10^{14}$  W/cm $^2$  is scaled down in the trailing pulse by (a) the factor  $\nu = 1$ , (b) 0.64, and (c) 0.36. The delay between the pulses  $\Delta t = 0$ .

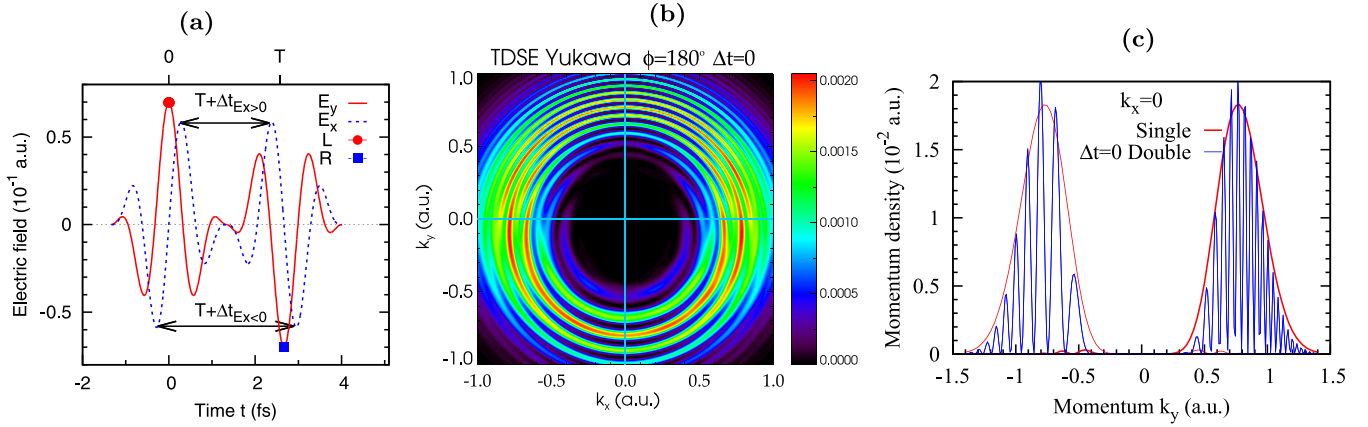


FIG. 5. Two-pulse interference in the Yukawa atom with the inverted trailing pulse. Both pulses have intensity of  $0.86 \times 10^{14}$  W/cm<sup>2</sup>. Panel (a) shows the electric-field diagram. The arrows indicate the peak-to-peak separation of the electric-field  $E_x > 0$  and  $E_x < 0$ . Panel (b) displays the PMD obtained with the pulse separation  $\Delta t = 0$ . Panel (c) exhibits the momentum density cut  $P(k_x = 0, k_y)$ . The envelopes are derived from the corresponding cut of the PMD obtained from a single pulse which is interference free.

correlation is exhibited in Fig. 6 on the absolute scale. The conspicuous maxima lying on the  $t_1 = t_2$  diagonal are the trivial same time self-correlation. Less obvious are the maxima at  $t_{1,2} \approx 0.5T$ ,  $t_{2,1} \approx t_1 + \Delta t$ . These maxima reflect correlation between the ionization events occurring at the maximum field strength of each pulse. An electron ionized at the peak field strength of the first pulse at  $t_1 \approx T/2$  experiences another boost when the electric field of the second pulse reaches its maximum at  $t_2 = t_1 + \Delta t$ . This is reflected in the observed correlation pattern.

## V. SUMMARY AND OUTLOOK

In this article, we demonstrate the photoelectron interference and the photon absorption rate correlation in the attoclock driven by two circularly polarized single-cycle pulses. The observed two-pulse interference is purely kinematic and only depends on the essential pulse and target parameters:  $T$ ,  $\Delta t$ ,  $U_p$ , and  $I_p$ . It is insensitive to the orbital structure of the target atom as was demonstrated for various  $3p_m$  initial states of the Ar atom. Reduction of the strength of the trailing pulse relative to its leading master changes the interference pattern profoundly. In addition, the relative phase of the leading and trailing (master and replica) pulses can be

inverted to create an asymmetric interference pattern which is very sensitive to the electric-field waveform.

Our technique does not provide a complete shot-to-shot pulse reconstruction that was recently demonstrated in the attoclock setting [39,40]. Nevertheless, it allows to gain some useful information on several important pulse parameters. In particular, it allows for an accurate determination of the ponderomotive energy or, equivalently, the pulse intensity which otherwise is difficult to determine for very short and intense pulses.

Besides the single-cycle pulse characterization, the two-pulse attoclock can be used to monitor the population dynamics in the target during the ionization process. Figure 7 displays the population depletion in the hydrogen atom subjected by the sequence of two identical single-cycle pulses at varying intensities. Although the weakest pulses at  $0.86 \times 10^{14}$  W/cm<sup>2</sup> hardly change the population of the initial  $1s$  state, the intensity increase to  $2.58 \times 10^{14}$  W/cm<sup>2</sup> depletes this population significantly. As the result, the ionization amplitudes entering Eq. (1) would differ substantially, and the two-pulse interference pattern would evolve from the fully

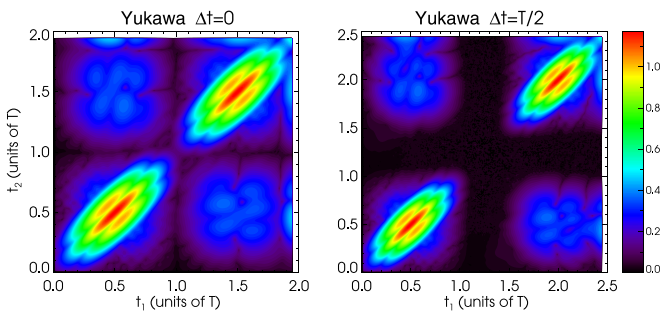


FIG. 6. Correlation between the photon absorption rates at different times in the Yukawa atom driven by two short  $N_c = 1$  pulses with  $I = 0.86 \times 10^{14}$  W/cm<sup>2</sup>,  $\epsilon = 1$ ,  $\lambda = 800$  nm and a fixed separation  $\Delta t = 0$  (left) and  $T/2$  (right).

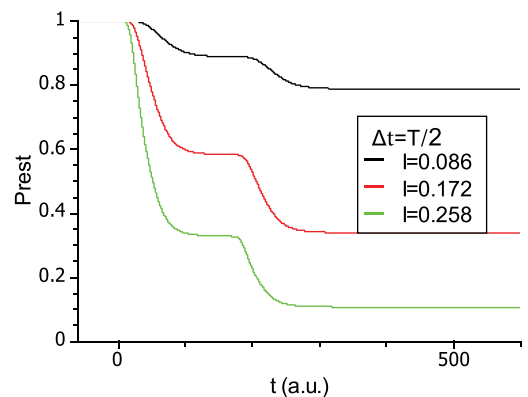


FIG. 7. The population depletion of the hydrogen atom by the sequence of two single-cycle pulses at various intensities  $I$  (in units of PW/cm<sup>2</sup> =  $1 \times 10^{15}$  W/cm<sup>2</sup>). The pulse separation  $\Delta t = T/2$ .

filled minima of Fig. 4(a) to the partially filled ones of Figs. 4(b) and 4(c). This provides a very direct way of monitoring the target repopulation evolution during the ionization process.

As a further direction, we studied the two-pulse attoclock interference in the  $H_2$  molecule. Even though the photoelectron spectra differ for various molecular orientations [41], the same universal interference pattern was detected irrespective of the molecular alignment. This universal pattern, however, could have been distorted had we included the propagation time of the laser pulse reaching the two constituent atoms at different instances. This effect has already been

observed in a synchrotron driven interference experiment on  $H_2$  [42,43]. We hope we will be able to demonstrate this effect in the  $H_2$  attoclock. A relativistic extension of the present techniques beyond the dipole approximation is needed to reach this goal. This development is currently underway [44].

#### ACKNOWLEDGMENTS

Technical support and resources of the National Computational Infrastructure Facility (NCI Australia) were used in the present paper.

- 
- [1] P. Salières, B. Carré, L. Le Déroff, F. Grasbon, G. G. Paulus, H. Walther, R. Kopold, W. Becker, D. B. Milošević, A. Sanpera *et al.*, Feynman's path-integral approach for intense-laser-atom interactions, *Science* **292**, 902 (2001).
- [2] O. Smirnova, Y. Mairesse, S. Patchkovskii, N. Dudovich, D. Villeneuve, P. Corkum, and M. Y. Ivanov, High harmonic interferometry of multi-electron dynamics in molecules, *Nature (London)* **460**, 972 (2009).
- [3] O. Pedatzur, G. Orenstein, V. Serbinenko, H. Soifer, B. D. Bruner, A. J. Uzan, D. S. Brambila, A. G. Harvey, L. Torlina, F. Morales *et al.*, Attosecond tunnelling interferometry, *Nat. Phys.* **11**, 815 (2015).
- [4] A. J. Uzan, H. Soifer, O. Pedatzur, A. Clergerie, S. Larroque, B. D. Bruner, B. Pons, M. Ivanov, O. Smirnova, and N. Dudovich, Spatial molecular interferometry via multidimensional high-harmonic spectroscopy, *Nat. Photonics* **14**, 188 (2020).
- [5] H. G. Muller and F. C. Kooiman, Bunching and Focusing of Tunneling Wave Packets in Enhancement of High-Order Above-Threshold Ionization, *Phys. Rev. Lett.* **81**, 1207 (1998).
- [6] F. Lindner, M. G. Schätzel, H. Walther, A. Baltuška, E. Goulielmakis, F. Krausz, D. B. Milošević, D. Bauer, W. Becker, and G. G. Paulus, Attosecond Double-Slit Experiment, *Phys. Rev. Lett.* **95**, 040401 (2005).
- [7] M. Okunishi, R. Itaya, K. Shimada, G. Prümper, K. Ueda, M. Busuladžić, A. Gazibegović, D. B. Milošević, and W. Becker, Two-Source Double-Slit Interference in Angle-Resolved High-Energy Above-Threshold Ionization Spectra of Diatoms, *Phys. Rev. Lett.* **103**, 043001 (2009).
- [8] M. Ivanov, in *Attosecond and XUV Spectroscopy: Ultrafast Dynamics and Spectroscopy*, 1st ed., edited by T. Schultz and M. Vrakking (Wiley-VCH, 2014), pp. 179–200.
- [9] P. Eckle, A. N. Pfeiffer, C. Cirelli, A. Staudte, R. Dorner, H. G. Muller, M. Buttiker, and U. Keller, Attosecond ionization and tunneling delay time measurements in helium, *Science* **322**, 1525 (2008).
- [10] P. Eckle, M. Smolarski, P. Schlup, J. Biegert, A. Staudte, M. Schöffler, H. G. Muller, R. Dorner, and U. Keller, Attosecond angular streaking, *Nat. Phys.* **4**, 565 (2008).
- [11] A. N. Pfeiffer, C. Cirelli, M. Smolarski, D. Dimitrovski, M. Abu-samha, L. B. Madsen, and U. Keller, Attoclock reveals natural coordinates of the laser-induced tunnelling current flow in atoms, *Nat. Phys.* **8**, 76 (2012).
- [12] A. S. Landsman, M. Weger, J. Maurer, R. Boge, A. Ludwig, S. Heuser, C. Cirelli, L. Gallmann, and U. Keller, Ultrafast resolution of tunneling delay time, *Optica* **1**, 343 (2014).
- [13] E. E. Serebryannikov and A. M. Zheltikov, Tunneling phase time in photoionization: in search of a clock, *Optica* **3**, 1201 (2016).
- [14] L. Torlina, F. Morales, J. Kaushal, I. Ivanov, A. Kheifets, A. Zielinski, A. Scrinzi, H. G. Muller, S. Sukiasyan, M. Ivanov *et al.*, Interpreting attoclock measurements of tunnelling times, *Nat. Phys.* **11**, 503 (2015).
- [15] U. S. Sainadh, H. Xu, X. Wang, A. Atia-Tul-Noor, W. C. Wallace, N. Douguet, A. Bray, I. Ivanov, K. Bartschat, A. Kheifets *et al.*, Attosecond angular streaking and tunnelling time in atomic hydrogen, *Nature (London)* **568**, 75 (2019).
- [16] A. S. Kheifets, The attoclock and the tunneling time debate, *J. Phys. B: At., Mol. Opt. Phys.* **53**, 072001 (2020).
- [17] U. S. Sainadh, R. T. Sang, and I. V. Litvinyuk, Attoclock and the quest for tunnelling time in strong-field physics, *J. Phys.: Photonics* **2**, 042002 (2020).
- [18] C. Hofmann, A. Bray, W. Koch, H. Ni, and N. I. Shvetsov-Shilovski, Quantum battles in attoscience: tunnelling, *Eur. Phys. J. D* **75**, 208 (2021).
- [19] E. Hasović, W. Becker, and D. B. Milošević, Electron rescattering in a bicircular laser field, *Opt. Express* **24**, 6413 (2016).
- [20] K.-J. Yuan, S. Chelkowski, and A. D. Bandrauk, Photoelectron momentum distributions of molecules in bichromatic circularly polarized attosecond UV laser fields, *Phys. Rev. A* **93**, 053425 (2016).
- [21] J. M. Ngoko Djiokap, A. V. Meremianin, N. L. Manakov, S. X. Hu, L. B. Madsen, and A. F. Starace, Multistart spiral electron vortices in ionization by circularly polarized UV pulses, *Phys. Rev. A* **94**, 013408 (2016).
- [22] D. Pengel, S. Kerbstadt, D. Johannmeyer, L. Englert, T. Bayer, and M. Wollenhaupt, Electron Vortices in Femtosecond Multiphoton Ionization, *Phys. Rev. Lett.* **118**, 053003 (2017).
- [23] S. Kerbstadt, K. Eickhoff, T. Bayer, and M. Wollenhaupt, Odd electron wave packets from cycloidal ultrashort laser fields, *Nat. Commun.* **10**, 658 (2019).
- [24] M. Seo, K. Tsendsuren, S. Mitra, M. Kling, and D. Kim, High-contrast, intense single-cycle pulses from an all thin-solid-plate setup, *Opt. Lett.* **45**, 367 (2020).

- [25] P. R. Ribic and T. Tanaka, Isolated single-cycle extreme-ultraviolet pulses from undulator radiation, *Opt. Lett.* **45**, 5234 (2020).
- [26] R. Della Picca, A. A. Gramajo, C. R. Garibotti, S. D. López, and D. G. Arbó, Nonconstant ponderomotive energy in above-threshold ionization by intense short laser pulses, *Phys. Rev. A* **93**, 023419 (2016).
- [27] M. Wickenhauser, X. M. Tong, and C. D. Lin, Laser-induced substructures in above-threshold-ionization spectra from intense few-cycle laser pulses, *Phys. Rev. A* **73**, 011401(R) (2006).
- [28] C. J. Joachain, N. J. Kylstra, and R. M. Potvliege, *Atoms in Intense Laser Fields* (Cambridge University Press, Cambridge, UK, 2011).
- [29] I. A. Ivanov, Evolution of the transverse photoelectron-momentum distribution for atomic ionization driven by a laser pulse with varying ellipticity, *Phys. Rev. A* **90**, 013418 (2014).
- [30] V. V. Serov, Calculation of intermediate-energy electron-impact ionization of molecular hydrogen and nitrogen using the paraxial approximation, *Phys. Rev. A* **84**, 062701 (2011).
- [31] I. Barth and O. Smirnova, Nonadiabatic tunneling in circularly polarized laser fields: Physical picture and calculations, *Phys. Rev. A* **84**, 063415 (2011).
- [32] D. B. Milošević, G. G. Paulus, D. Bauer, and W. Becker, Above-threshold ionization by few-cycle pulses, *J. Phys. B: At., Mol. Opt. Phys.* **39**, R203 (2006).
- [33] S. G. Johnson, The NLOpt nonlinear-optimization package, <http://github.com/stevengj/nlopt>
- [34] L. Mandel and E. Wolf, *Optical Coherence and Quantum Optics* (Cambridge University Press, Cambridge, UK, 1995).
- [35] I. A. Ivanov and K. T. Kim, Simple man model in the Heisenberg picture, *Commun. Phys.* **3**, 7 (2020).
- [36] I. A. Ivanov, A. S. Kheifets, and K. T. Kim, Time correlation inside a laser pulse, *Phys. Rev. A* **101**, 043407 (2020).
- [37] I. A. Ivanov and K. T. Kim, Atomic ionization driven by the quantized electromagnetic field in a Fock state, *Phys. Rev. A* **102**, 023117 (2020).
- [38] V. V. Serov, J. Cesca, and A. S. Kheifets, Numerical and laboratory attoclock simulations on noble-gas atoms, *Phys. Rev. A* **103**, 023110 (2021).
- [39] S. Li, Z. Guo, R. N. Coffee, K. Hegazy, Z. Huang, A. Natan, T. Osipov, D. Ray, A. Marinelli, and J. P. Cryan, Characterizing isolated attosecond pulses with angular streaking, *Opt. Express* **26**, 4531 (2018).
- [40] N. Hartmann, G. Hartmann, R. Heider, M. S. Wagner, M. Ilchen, J. Buck, A. O. Lindahl, C. Benko, J. Grünert, J. Krzywinski *et al.*, Attosecond time-energy structure of x-ray free-electron laser pulses, *Nat. Photonics* **12**, 215 (2018).
- [41] V. V. Serov, A. W. Bray, and A. S. Kheifets, Numerical attoclock on atomic and molecular hydrogen, *Phys. Rev. A* **99**, 063428 (2019).
- [42] S. Grundmann, D. Trabert, K. Fehre, N. Strenger, A. Pier, L. Kaiser, M. Kircher, M. Weller, S. Eckart, L. P. H. Schmidt *et al.*, Zeptosecond birth time delay in molecular photoionization, *Science* **370**, 339 (2020).
- [43] H. Liang, S. Grundmann, Y.-K. Fang, L. Geng, Q. Gong, and L.-Y. Peng, Nondipole effects in interference patterns of a two-electron wave, *Phys. Rev. A* **104**, L021101 (2021).
- [44] I. A. Ivanov, A. S. Kheifets, and K. T. Kim, Effect of the finite speed of light in ionization of extended systems, [arXiv:2106.14382](https://arxiv.org/abs/2106.14382).